

Understanding, predicting, and tuning the fragility of vitrimeric polymers

Simone Ciarella^{a,1}, Rutger A. Biezemans^a, and Liesbeth M. C. Janssen^{a,2}

^aTheory of Polymers and Soft Matter, Department of Applied Physics, Eindhoven University of Technology, Den Dolech 2, 5600 MB Eindhoven, The Netherlands

This manuscript was compiled on October 2, 2019

Fragility is an empirical property that describes how abruptly a glass-forming material solidifies upon supercooling. The degree of fragility carries important implications for the functionality and processability of a material, as well as for our fundamental understanding of the glass transition. However, the microstructural properties underlying fragility still remain poorly understood. Here, we explain the microstructure-fragility link in vitrimeric networks, a novel type of high-performance polymers with unique bond-swapping functionality and unusual glass-forming behavior. Our results are gained from coarse-grained computer simulations and first-principles Mode-Coupling Theory (MCT) of star-polymer vitrimers. We first demonstrate that the vitrimer fragility can be tuned over an unprecedentedly broad range, from fragile to strong and even superstrong behavior, by decreasing the bulk density. Remarkably, this entire phenomenology can be reproduced by microscopic MCT, thus challenging the conventional belief that existing first-principles theories cannot account for non-fragile behaviors. Our MCT analysis allows us to rationally identify the microstructural origin of the fragile-to-superstrong crossover, which is rooted in the sensitivity of the static structure factor to temperature variations. On the molecular scale, this behavior stems from a change in dominant length scales, switching from repulsive excluded-volume interactions to intrachain attractions as the vitrimer density decreases. Finally, we develop a simplified schematic MCT model which corroborates our microscopically-founded conclusions and which unites our findings with earlier MCT studies. Our work sheds new light on the elusive structure-fragility link in glass-forming matter, and provides a first-principles-based platform for designing novel amorphous materials with an on-demand dynamic response.

Keyword 1 | Keyword 2 | Keyword 3 | ...

Vitrimeric polymers are a new class of polymer glasses with exceptional material properties, combining the malleability and recyclability of thermoplastics with the high mechanical performance of thermosets (1, 2). Their unique processability stems from a reversible bond-exchange mechanism, which allows covalent crosslinks in the polymer network to change dynamically whilst preserving the total number of bonds. In effect, vitrimers can thus behave as viscoelastic liquids at high temperatures, and as crosslinked thermosets at low temperatures. Importantly, the relaxation dynamics of vitrimers is characterized by two distinct transition temperatures: a conventional glass transition temperature T_g at which the material undergoes kinetic arrest, and a topology-freezing transition temperature T_v at which the bond-switching rate becomes immeasurably slow. The latter transition temperature can be controlled independently from T_g , e.g. by tuning the concentration of catalyst for the exchange reaction (3).

A widely employed classification scheme for glass-forming matter, proposed by Angell (4), is based on the fragility—a

measure for how rapidly the relaxation dynamics of a material slows down upon approaching the glass transition. The fragility index m can be defined as $m = d \log_{10} \tau / d(T_g/T)|_{T=T_g}$, where τ is the structural relaxation time and T is the temperature. For so-called 'strong' glass formers, the relaxation-time growth near T_g follows an Arrhenius law, while for 'fragile' glass formers the relaxation time increases more abruptly upon cooling (super-Arrhenius behavior), giving rise to larger values of m . These differences in the fragility index are important for two reasons. First, the concept of fragility offers a unifying framework to classify seemingly disparate classes of glass-forming matter, ranging from atomic liquids (4) to colloidal (5) and cellular systems (6). As such, it is paramount to an ultimately universal description of the glass transition. Second, the fragility index of a material directly impacts its functionality and processability: a low m , for example, generally implies a broader glass transition temperature range, increasing the ease with which a material can be molded. Remarkably, while most polymers are fragile (7), vitrimers exhibit an even lower fragility index than the prototypical strong glass former silica (2), rendering them 'superstrong' and highly suitable for (re)processing. Despite both the fundamental and practical importance of fragility, however, there is still no detailed understanding of the physical mechanisms underlying this phenomenon, and a predictive theory that can rationally link the observed fragility to a material's microstructure is still lacking (8–14). This constitutes not only a major fundamental problem, but it also impedes any rational approach toward the development of sustainable, high-performance amorphous

Significance Statement

The intricate interplay between the molecular structure of a material and its emergent macroscopic dynamics lies at the heart of modern materials science. This interplay, however, remains notoriously poorly understood for glass-forming systems. The recent advent of vitrimers—a promising new class of recyclable high-performance polymers with anomalous glass-forming properties—revives the urgency to gain a full understanding of the elusive structure-dynamics link in glassy matter. We combine computer simulations and first-principles theory to rationally expose the structural origins of the complex glassy dynamics in vitrimers. Our findings provide cues for a better fundamental understanding of glass formation, and may stimulate the development of novel, sustainable amorphous materials with on-demand functionalities.

Please provide details of author contributions here.

Please declare any conflict of interest here.

E-mail: ¹S.Ciarella@tue.nl ²L.M.C.Janssen@tue.nl

materials with an on-demand dynamic response.

Empirical studies over the last few decades have nonetheless yielded valuable insight into the molecular and microstructural origins of fragility. It is now well established that network-forming materials such as silica, which are characterized by anisotropic interactions, tend to behave as strong glass formers (15, 16), while fragile materials are often governed by isotropic and excluded-volume interactions (17, 18). In dense colloidal suspensions, the fragility is also intimately related to the particle softness (19), roughness (20), elasticity (5, 21–23), and confinement effects (24). For polymeric systems, the glassy dynamics is generally more complex, owing to the competition between intra- and interchain degrees of freedom (25, 26). A recent study (7) argues that in fragile polymers with high molecular weights, the slow intrachain (segmental) relaxation dynamics can give rise to unusually high values of m , even though the interchain relaxation may remain comparable to that of moderately fragile liquids. Finally, the liquid fragility also correlates well with material properties deep in the glass phase, in particular the vibrational properties and nonergodicity factor at temperatures well below T_g (27).

From the theoretical side, it is widely accepted that material-dependent dynamical properties such as the fragility must ultimately be related to structural ones (28). After decades of intense research, there now exist numerous theories of the glass transition that aim to rationalize the observed fragility for a given material composition and structure, notably including Random First Order Transition Theory (RFOT) (29), geometric frustration (30, 31), and Mode-Coupling Theory (MCT) (32, 33). Among these, MCT stands out as the only theory that is founded entirely on first principles. As such, MCT seeks to predict the full microscopic relaxation dynamics of a glass-forming system (as a function of time, temperature, density, and wavenumber k) in a semi-quantitative way (34, 35) based solely on knowledge of simple structural material properties such as the static structure factor $S(k)$. However, even though experiments suggest that subtle features in $S(k)$, especially in the main peak at wavenumber $k = k_0$, may correlate well with the fragility index (36), MCT often fails to give an accurate prediction of the observed fragility. In fact, due to the inherent mathematical form of the MCT equations, the theory is only capable of predicting a fragile (power-law) divergence of τ near the MCT glass transition. Indeed, a 2011 review contemplated that a quantitative account of fragility from a purely first-principles microscopic theory remains, thus far, only a “dream” (11).

Here we challenge this status quo by elucidating and predicting the fragility of vitrimeric polymers using coarse-grained Molecular Dynamics (MD) simulations and MCT. We first demonstrate that, within our vitrimeric model system, the fragility index can be tuned over an unprecedentedly broad range, from fragile super-Arrhenius to superstrong sub-Arrhenius behavior, by tuning the bulk density. Furthermore, we find that the fragility does not change with the swap rate, suggesting that the observed phenomenology is more related to the intrinsic structure of the liquid rather than the swap-dependent dynamics. Remarkably, we can reproduce and predict this entire range of fragilities from microscopic MCT, using only the static structure factors at the corresponding temperatures and densities as input. Our first-principles MCT analysis allows us to rationalize the observed crossover from

fragile to superstrong behavior in terms of a change in dominant length scales, which switches from inter- to intrachain interactions as the density decreases. Moreover, we can directly attribute the fragility at a given density to the growth behavior of the static structure factor: at low densities, anomalously strong vitrimers are governed by an anomalously weak variation of $S(k)$ upon cooling. This new insight finally allows us to develop a simple schematic (wavevector-independent) MCT model which not only recovers our fully microscopic MCT predictions, but which also reveals how our MCT-predicted fragility range can be united with MCT’s well-established fragile power-law divergence. Overall, this work sheds new light on the microstructural origins of fragility, and uncovers a previously unknown application domain for a near-quantitative first-principles theory of glassy dynamics. The here established rational link between molecular length scales on the one hand, and the macroscopic material response on the other hand, may also guide ongoing experimental efforts to design and optimize new structural glasses with tunable dynamic functionalities.

1. Approach

Our results are gained from MD simulations, which serve as ‘numerical experiments’, combined with theoretical predictions from both fully microscopic and schematic MCT. The simulation model consists of a binary mixture of star polymers, inspired by the system used in Ref. (37) (see Fig. 1 and Materials and Methods). The star-shaped structure, which is comparable to soft colloids (38–40), offers a complex scenario for fragility (5, 19–23), on top of tunable mechanics (41). Briefly, the monomer segments are connected through harmonic springs with equilibrium length L_0 ; steric repulsion among non-nearest-neighbor segments is implemented through a Weeks-Chandler-Andersen (WCA) potential with cutoff radius $\sigma = 0.9L_0$. Importantly, the monomers at the ends of the arms are functionalized such that they can form attractive bonds which can swap reversibly, thus endowing them with vitrimeric functionality (37, 42). For these attractive end-segment interactions, we use a generalized 20-10 Lennard-Jones potential with minimum energy $\epsilon \gg k_B T$, where k_B is the Boltzmann constant. We assume that every bond-swapping reaction requires an activation energy ΔE_{swap} , which experimentally can be controlled by e.g. the amount of catalyst. Physically, by varying ΔE_{swap} , we can thus tune the location of the topology-freezing transition temperature T_v independently from T_g . In the remainder of this paper, we adopt reduced units for the length, energy, and monomer mass such that $L_0 = 1$, $\epsilon = 1$, and $m_0 = 1$, respectively; the temperature T is defined in units of ϵ/k_B .

To quantify the time-dependent glassy relaxation dynamics, we measure the monomer-averaged self- and collective intermediate scattering functions (26) $F_s(k, t) = N^{-1} \langle \sum_{j=1}^N \exp[-i\mathbf{k} \cdot (\mathbf{r}_j(0) - \mathbf{r}_j(t))] \rangle$ and $F(k, t) = N^{-1} \langle \sum_{j,l=1}^N \exp[-i\mathbf{k} \cdot (\mathbf{r}_j(0) - \mathbf{r}_l(t))] \rangle$, where N is the total number of monomers, \mathbf{k} is a wavevector of magnitude k , $\mathbf{r}_j(t)$ denotes the position of monomer j at time t , and the brackets $\langle \dots \rangle$ represent an ensemble average. Note that this monomer-averaged approximation, which has been successfully applied to coarse-grained glassy polymers (25, 26, 43–45), would correspond in experiment to the case where all segments have identical scattering form factors. The vitrimer microstructure is quantified by the average static structure

factor $S(k) = N^{-1} \langle \sum_{j,l=1}^N \exp[-i\mathbf{k} \cdot (\mathbf{r}_j(0) - \mathbf{r}_l(0))] \rangle$. We define the structural relaxation time τ as $F_s(k_0, \tau) = e^{-1}$ and the operational glass transition temperature T_g as the temperature below which $F_s(k, t)$ fails to decay within the maximum simulation time of $10^{4.5} \tau_0$, i.e. $\tau(T_g) = 10^{4.5} \tau_0$. Here τ_0 is the structural relaxation time of a reference fluid state at density $\rho = 1.58$ and temperature $T = 0.2$, which corresponds to $\tau_0 = 0.06[(m_0 L_0^2 / \epsilon)^{1/2}]$. The fragility index m can subsequently be extracted from $\tau(T_g)$ for any given density. To investigate the role of the topology-freezing transition temperature T_v , we perform simulations both for $\Delta E_{\text{swap}} = 0$, implying barrierless bond swaps, and $\Delta E_{\text{swap}} = \infty$, implying $T_v \gg T \geq T_g$.

In order to elucidate the link between the vitrimer microstructure and its time-dependent relaxation dynamics, we invoke fully microscopic (k -dependent) Mode-Coupling Theory (see Materials and Methods). Briefly, MCT amounts to a first-principles-based non-linear equation for the dynamic intermediate scattering function, which can be solved self-consistently once the static structure factor $S(k)$ for a given temperature and density is known (32, 46). Though it is well known that MCT is not exact (47), and is generally only quantitatively accurate at temperatures well above T_g , the theory allows us to identify—at least qualitatively—which microstructural features dominate the glassy dynamics manifested in $F_s(k, t)$ and $F(k, t)$. As detailed below, our theoretical analysis reveals a direct correlation between the broad fragility range of vitrimers and the particular sensitivity of $S(k)$ to temperature variations, effectively captured by the anomalous growth of the structure factor peak $S(k = k_0)$. To unambiguously confirm this unique structure-fragility link, we also develop a minimal MCT model that takes into account only the growth of $S(k_0)$; by showing that the model can reproduce all qualitative features of the fully microscopic MCT predictions, we can thus rationally establish how different apparent fragilities emerge from different microstructures.

2. Results

A. Dynamics from numerical simulation. We first discuss the vitrimer relaxation dynamics obtained from simulation. Figure 2(a) shows the Angell plot of the structural relaxation times τ as a function of normalized inverse temperature, evaluated at the peak k_0 . It can be seen that high-density vitrimers ($\rho \geq 2.0$) exhibit a relatively steep growth of τ upon supercooling, indicative of fragile glass formation, while intermediate densities ($1.5 < \rho < 2.0$) yield an Arrhenius form that is characteristic of strong network-forming materials. Notably, as the bulk density decreases even further ($\rho < 1.5$), the vitrimer melt approaches the glass transition with remarkably weak temperature dependence—a sub-Arrhenius behavior which we designate as superstrong. The respective glass transition temperatures change from $T_g \approx 10^{-1}$ at high densities to $T_g \approx 10^{-6}$ at the lowest densities studied. In Fig. S2 we show the same plot for different values of k , confirming that the fragility is k -independent.

To quantify the observed fragility, we also plot the fragility indices m as a function of bulk density in Fig. 2(f); the m values are derived from polynomial fitting of the data in Fig. 2(a). The superstrong functionality at low densities is manifested in the anomalously low values of m , revealing an essentially constant fragility of $m \approx 1$ for $\rho_c \leq 1.5$. As the density

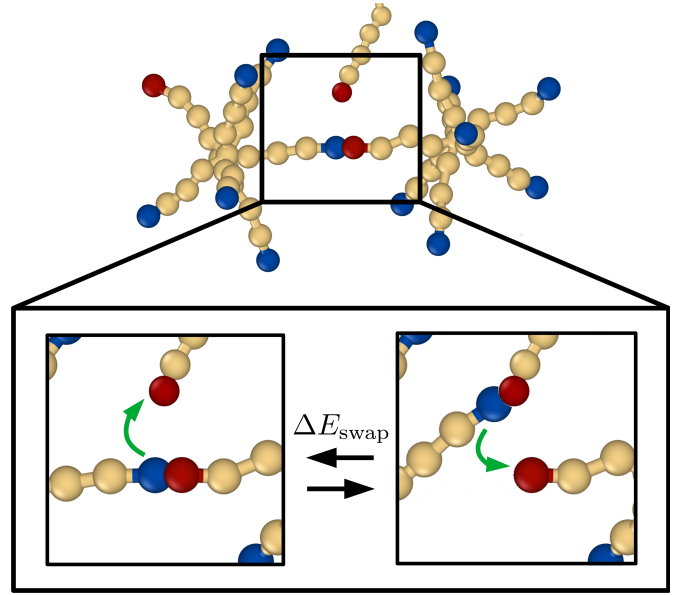


Fig. 1. Illustration of the vitrimer simulation model. The system is composed of a mixture of 8-arm star polymers, the monomer ends of which (shown as blue and red beads) are capable of forming swappable vitrimeric bonds. The activation energy barrier for a bond-swap event is ΔE_{swap} ; in our simulations, we can tune the value of ΔE_{swap} between 0 and ∞ .

increases beyond ρ_c , the fragility index increases monotonically and the material becomes increasingly more fragile. Hence we may conclude that, for our vitrimer simulation model, the bulk density provides a thermodynamic control parameter to tune the fragility from superstrong to strong to fragile.

The influence of T_v can be seen in the (ρ, T) phase diagram of Fig. 2(e). Our simulations reveal two different amorphous phases: an ergodic phase in which $F_s(k, t)$ fully decays to zero within the time scale of simulation (marked as ‘fluid’ in Fig. 2(e)), and a solid glass phase in which $F_s(k, t)$ remains finite such that $\tau \geq 10^{4.5} \tau_0$. For all the (ρ, T) state points considered here, the star polymers form a network kept together by the functionalized attractive end segments. Our mixture composition ensures that the maximum number of inter-star bonds (set by the minority end species, see Materials and Methods) is below the rigidity transition (48–50), so that the system can relax without undergoing bond swaps; this is confirmed by our $\Delta E_{\text{swap}} = \infty$ results. Furthermore, this mixture choice allows us to explicitly decouple the glass transition T_g from the topology-freezing transition temperature T_v : we can reach T_g for both $T_g < T_v$ and $T_g > T_v$. Note that in the earlier work of Ref. (37), the relaxation time would diverge at T_v (3) such that $T_g = T_v$. Figure 2(e) shows the ergodic-to-glass transition line (i.e., the density-dependent values of T_g) for the two extreme cases of $\Delta E_{\text{swap}} = 0$ and $\Delta E_{\text{swap}} = \infty$, implying topology-freezing transition temperatures of $T_v \rightarrow 0$ and $T_v \rightarrow \infty$, respectively. It can be seen that, while the shape of the two transition lines is similar, the introduction of reversible bond swaps ($\Delta E_{\text{swap}} = 0$) shifts the glass transition to lower temperatures and higher densities. Thus, for a given T_g , decreasing T_v leads to a higher critical density at which vitrification occurs, and therefore to a melting of the glass within the gray-shaded region of Fig. 2(e). This effect is not surprising, as enhanced vitrimeric functionality is known to lead to more efficient relaxation and more liquid-like behavior

(37, 51). Interestingly, we find that the fragility index m along the glass transition line is virtually unaffected by our choice of ΔE_{swap} (Fig. S4), implying that the fragility is determined by intrinsic star polymer properties, rather than by bond-swapping events. Since the quantitative difference between $T_v \rightarrow 0$ and $T_v \rightarrow \infty$ in the phase diagram is relatively minor, we focus in the remainder of the paper only on the data for $\Delta E_{\text{swap}} = 0$, for which we have better statistics.

B. Dynamics from Mode-Coupling Theory. Let us now investigate how certain properties of the microstructure may underlie and explain the unusually broad fragility range observed in simulation. To this end, we perform a theoretical analysis based on MCT, in which we use the simulated static structure factors $S(k)$ at a given (ρ, T) state point as input to predict the full dynamics. While decades of research have firmly established that MCT can only predict a fragile power-law divergence of τ near the MCT critical point (32, 52), the microstructural information encoded in $S(k)$ may be sufficient to account at least qualitatively for the observed differences in fragility indices (53, 54). The results of our microscopic, fit-parameter-free MCT calculations for the single-particle dynamics are shown in the Angell plot of Fig. 2(b). Similar plots for the collective dynamics are presented in Fig. S3. We first point out that the respective T_g values used in the Angell plot are obtained from MD simulations; these temperatures need not coincide with the MCT-predicted glass transition $T_{g,MCT}$. In fact, we find that MCT predicts liquid-like behavior at all the state points considered in simulation, implying that the vitrimeric MCT transition temperature must lie *below* the simulated T_g . This finding is also consistent with other site-averaged MCT polymer studies (25, 55, 56). Based on extrapolation into the glassy regime (dashed lines in Fig. 2(b)), we estimate that $T_{g,MCT} \approx 0.5T_g$ for the most fragile samples. In order to enable a fair comparison between the MCT and simulation data in the well-equilibrated regime, we also present rescaled Angell plots in Figs. 2(c) and (d), corresponding to temperatures up to $0.5T_g$ in simulation and $\sim 0.5T_{g,MCT}$ in MCT, respectively.

The MCT results in Fig. 2 show that, despite the underestimation of the glass transition temperature, the theory is remarkably successful at capturing all *qualitative* features of the Angell plot. Indeed, in agreement with simulation, MCT predicts fragile-like behavior at high vitrimer densities, and strong and even anomalously superstrong behavior at low bulk densities. This trend is already observed in the high-temperature regime (Figs. 2(c,d)), in which all MCT-input structures are properly equilibrated. The MCT data in the glassy regime, obtained from fit-parameter-free MCT calculations using the simulated $T < T_g$ static structure factors as input (dashed lines in Fig. 2(b)), indicate a continuation of the same fragility trend. However, it must be noted that this MCT extrapolation inherently suffers from quantitative inaccuracies, as the corresponding microstructures at $T < T_g$ are poorly equilibrated. Moreover, our microscopic MCT analysis is based on monomer-averaged (structural and dynamical) correlation functions; an explicit multi-component treatment that distinguishes between different monomer species would possibly yield a higher MCT glass transition temperature $T_{g,MCT}$ (25, 55). Nonetheless, the fact that MCT manifestly predicts different growth behaviors of $\tau(T)$ for different bulk densities, consistent with simulation, suggests that MCT can provide a meaningful framework to elucidate the non-trivial structure-

fragility link in vitrimers. To complete our comparison, we also present the MCT fragility indices m , extracted from the most glassy MCT data of Fig. 2(b). As can be seen in Fig. 2(f), these MCT results are also in good qualitative agreement with numerical experiment across the entire density range studied. Notably, MCT accurately reproduces the crossover density $\rho_c \approx 1.5$ at which the vitrimer fragility changes from superstrong to strong.

At first glance, the fact that microscopic MCT can predict the full fragility range of our vitrimer system may seem at odds with the fragile power-law divergence expected from MCT on general mathematical grounds. However, as we discuss below and confirm explicitly using a schematic MCT model, such a divergence appears only sufficiently close to the MCT glass transition temperature $T_{g,MCT}$. For the vitrimer system under study, the MCT critical point falls outside the (ρ, T) domain accessible in simulation, rendering the theory capable of predicting *manifestly* different fragilities. We now use these MCT results to establish—on a rational, first-principles basis—which specific features of $S(k)$ underlie the observed fragility range of vitrimers.

C. Linking structure to fragility. The key structural quantity in our analysis is the monomer-averaged static structure factor $S(k)$, which probes static correlations between two density modes at wavenumber k . In simple glass-forming systems, the slowest (i.e. most glassy) density modes correspond to the main peak of $S(k)$, i.e., $k_0 \approx 2\pi/\sigma$, where σ denotes the typical monomer-particle diameter. MCT provides a general interpretation of this phenomenon in terms of the cage effect (57, 58): as $S(k_0)$ grows upon vitrification, particles become more confined within local cages formed by their nearest neighbors. This local dynamic slowdown, in turn, drives the slowdown at all other length scales via non-linear mode coupling, ultimately resulting in complete kinetic arrest. On the other hand, network-forming systems may be governed by larger length scales that are related to, e.g., the intrinsic network topology or crosslinker distance (51). Hence, to elucidate the dominant microstructural origin of the observed fragility of vitrimers, we must consider the structure and dynamics at both k_0 and smaller values of k .

Figure 3 shows the explicit k -dependence of both the structural relaxation times and the vitrimeric static structure factors for several densities and temperatures in the well-equilibrated regime. Let us first consider the single-particle relaxation times $\tau(k)$ and the collective analogues $\tau_c(k)$ in Figs. 3(a) and (b), respectively, which are defined as $F_s(k, \tau) = e^{-1}$ and $F(k, \tau_c) = e^{-1}$. Interestingly, while the self-dynamics is the slowest at low k -values for all densities considered, the *collective* dynamics in Fig. 3(b) reveals a more complex k -dependent picture (59). We find that fragile high-density systems are governed by the typical caging mode at k_0 , essentially conforming to simple glass-forming behavior (red lines in Fig. 3(b)), whereas superstrong low-density systems lack a notable dynamic signature at k_0 and are dominated by low- k modes instead (green lines in Fig. 3(b)). This trend, i.e. the relative decrease of $\tau_c(k_0)$ with decreasing fragility, is observed both in simulation and in full MCT. Since the single-particle dynamics is enslaved to the collective relaxation dynamics, these qualitative differences in collective k -dependent relaxation indicate an important change in the underlying relaxation mechanism: as the bulk density decreases and the material becomes stronger,

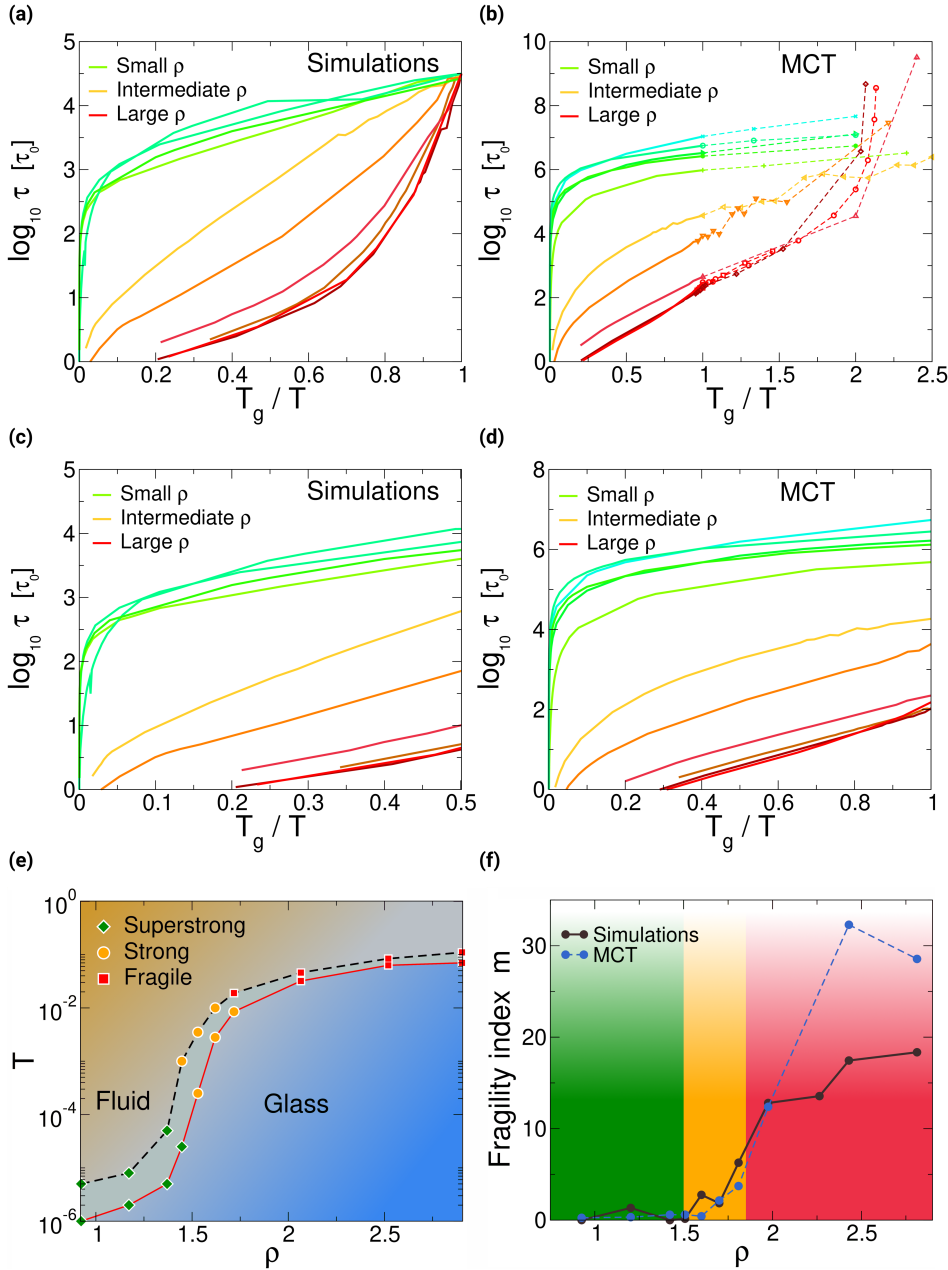


Fig. 2. (a,b) Angell plot of the structural relaxation time τ versus normalized inverse temperature, evaluated at the peak k_0 . Data are obtained from (a) MD simulations and (b) fit-parameter-free microscopic MCT. Different curves correspond to different bulk densities. The activation barrier for bond swapping was set to $\Delta E_{swap} = 0$. In both panels, the glass transition temperature T_g is set as the temperature at which the simulated system falls out of equilibrium such that $\tau = 10^{4.5} \tau_0$. (c) Same MD data as in (a), with the temperature axis limited to $0.5T_g$. (d) Same MCT data as in (b), with the temperature axis limited to T_g . We estimate that $T_{g,MCT} \approx 0.5T_g$ for the most fragile samples. (e) Simulated phase diagram as a function of temperature T and bulk density ρ . The phase labeled as 'fluid' corresponds to an underconstrained network of stars in which the dynamics is still ergodic such that $\tau < 10^{4.5} \tau_0$. The phase labeled as 'glass' corresponds to the non-ergodic phase with $\tau > 10^{4.5} \tau_0$. The black dashed line corresponds to $\Delta E_{swap} = \infty$ and the red line to $\Delta E_{swap} = 0$. The region shaded in grey indicates the regime in which the glass can be melted by vitrimeric bond swaps. (f) Fragility indices m as a function of bulk density ρ , obtained from polynomial fitting of the simulated and MCT-predicted Angell plots (panels a and b) near the respective glass transition temperatures. The regions shaded in green, orange, and red correspond to superstrong, strong, and fragile behavior, respectively.

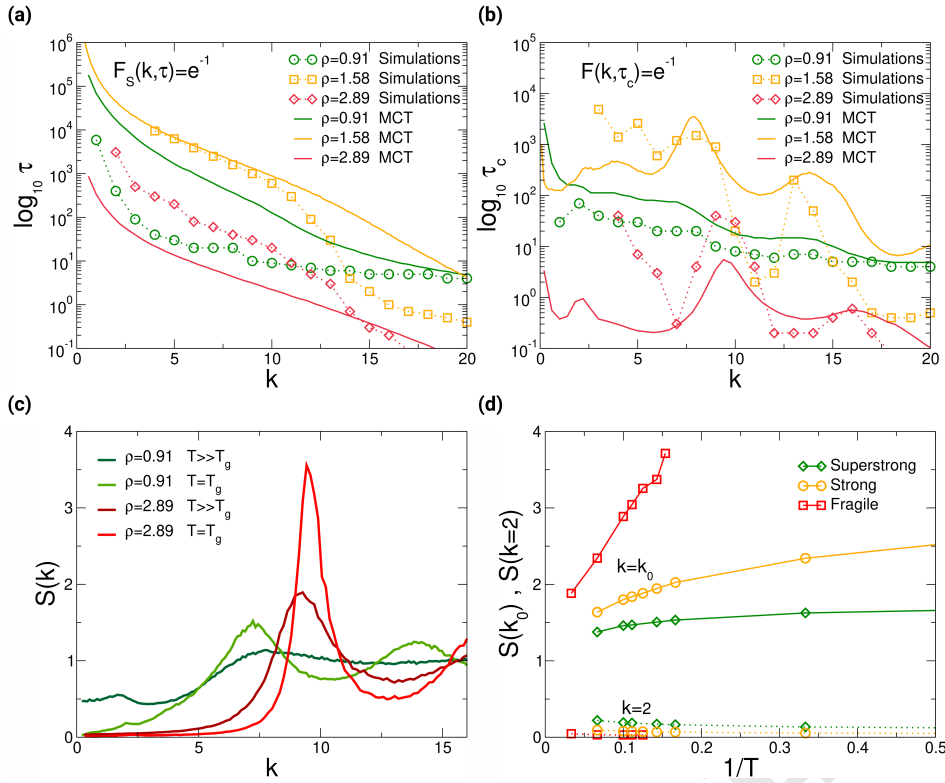


Fig. 3. (a) Averaged single-particle relaxation times τ as a function of wavenumber k for different densities at temperatures close to T_g , obtained from simulation (dotted lines) and full MCT (solid lines). (b) Collective relaxation times τ_c as a function of wavenumber k for the same densities and temperatures as in panel (a), obtained from simulation (dotted lines) and full MCT (solid lines). (c) Static structure factors for high-density ($\rho = 2.89$) and low-density ($\rho = 0.91$) vitrimers, measured both close to the glass transition temperature and well above T_g . The main peak shifts towards smaller k upon decreasing the bulk density of the system. (d) Temperature-dependent change in the value of $S(k)$ along different isochores, measured at both the main peak position k_0 (solid lines) and $k = 2$ (dotted lines). By supercooling the vitrimer system at constant density, the peak growth at k_0 is most pronounced at high density ($\rho = 2.89$), and becomes weaker when the density decreases (orange line, $\rho = 1.58$). At low density ($\rho = 0.91$), the temperature-dependent growth of the peak is remarkably weak.

the role of the conventional cage effect associated with k_0 diminishes. The fact that MCT also qualitatively predicts this change on first-principles grounds clearly suggests that the key explanation for this unusual phenomenology must lie in $S(k)$.

Figure 3(c) shows the full $S(k)$ curves for several representative vitrimer samples. We first note that the location of the $S(k_0)$ peak shifts toward lower wavenumbers and that the value of $S(k \rightarrow 0)$ increases as the density decreases. The latter is also consistent with the fact that a low-density polymeric network should have a relatively high compressibility. However, we find that the growth behavior of the $S(k_0)$ peak height upon supercooling is qualitatively different for low- and high-density vitrimers. As can be seen in Fig. 3(d), fragile vitrimers at high densities exhibit a relatively dramatic $S(k_0)$ temperature response and vitrify over a narrow temperature range. This abrupt growth of $S(k_0)$ is similar to the fragile behavior of, e.g., compressed hard spheres; indeed, we have verified that isothermal compression in our vitrimer model also yields a fragile growth of τ upon approaching the glass transition density, both in simulation and in MCT (see Fig. S5). Conversely, at low densities, the $S(k_0)$ height becomes remarkably insensitive to changes in the temperature, growing only very weakly across the entire range of supercooling accessible in simulation. In fact, the temperature-dependent change in $S(k_0)$ for these superstrong samples is almost comparable in magnitude to the $S(k)$ change at much lower wavenumbers. Based on this analysis, we can thus conclude that the diminishing of the cage effect in low-density vitrimers, and the corresponding emergence of superstrong fragilities, is rooted in the anomalously weak temperature-dependent variation of the static structure factor peak $S(k_0)$.

To gain a deeper structural understanding of the broad tunability of the vitrimer fragility with bulk density, let us

consider the real-space microstructure as probed by the radial distribution function $g(r)$. Its main peak represents the dominant nearest-neighbor interparticle distance r_0 that ultimately governs the value of $S(k_0)$ and, consequently, the strength of the cage effect and the sensitivity to temperature. Figure 4 shows the values of r_0 as a function of vitrimer bulk density at the respective glass transition temperatures T_g . At high densities, in which case the vitrimers exhibit fragile behavior, r_0 corresponds to length scales smaller than 0.9, where 0.9 sets the range of our WCA interaction potential. That is, the dominant nearest-neighbor interactions arise from steric repulsions among monomer segments, akin to the (fragile) excluded-volume-dominated vitrification scenario in dense hard spheres (60, 61). At low densities, however, r_0 approaches the equilibrium distance of the harmonic-spring potential that connects the monomers within each star-polymer arm. In this limit, the intrinsic topology of the star-polymer system thus plays a dominant role, and the structure resembles that of a strong network material such as silica (62). Since there are well defined ground states corresponding to fully bonded networks, the topology-dominated microstructure changes more weakly than in the steric-repulsion-dominated case, and consequently the static structure factor saturates more quickly upon supercooling. Hence, the low-density material behaves as a superstrong glass former. Notice that the absence of a sharp transition for low-density low-valence networks is consistent with the concept of “equilibrium gels” (63) where the glass transition approaches $T = 0$. The intermediate-density regime falls in between these two extreme cases, combining both topology-dominated (superstrong) and excluded-volume-dominated (fragile) interactions to yield intermediate fragility indices. Lastly, this analysis also explains why the value of the topology-freezing transition temperature T_v does not have

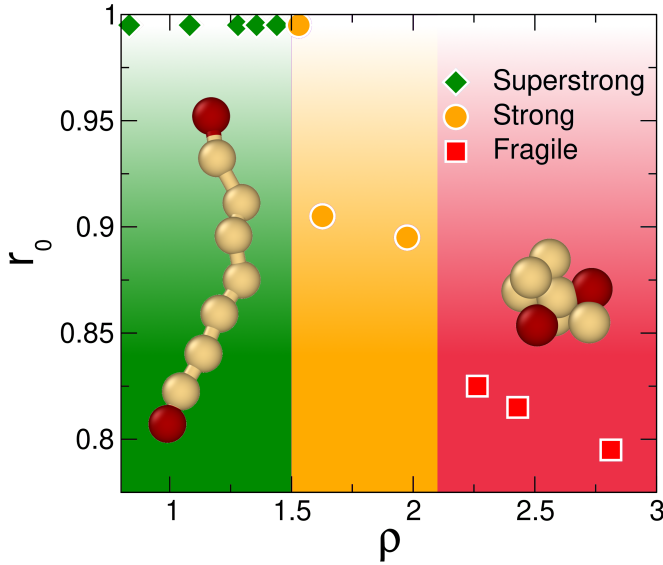


Fig. 4. Distance r_0 corresponding to the main peak of the radial distribution function $g(r)$ as a function of vitrimer bulk density. At low densities (green-shaded region), in which the system behaves as a dilute network of star polymers, the dominant length scale r_0 is set by the equilibrium length L_0 of the intra-star harmonic bonds. As the density increases (orange-shaded region), excluded-volume interactions become more dominant, resulting in a r_0 that is close to the repulsive WCA interaction range $\sigma = 0.9L_0$. At the highest densities studied (red-shaded region), segments are compressed to beyond the σ interparticle distance, resulting in $r_0 \approx 0.8L_0$.

a large influence on the fragility: reversible bond swaps occur only at the ends of the star-polymer arms, while the vast majority of monomer-monomer interactions—which ultimately control the dominant length scale—are unaffected by such bond-swapping events.

3. Schematic MCT analysis

To unambiguously confirm whether the growth behavior of the main peak of the static structure factor is indeed sufficient to classify the fragility of the material, and to unite our theoretical results with the well-established power-law divergence of microscopic MCT, we develop a schematic MCT model that relies solely on the functional form of $S(k_0)$ upon supercooling. Although schematic MCT models inherently lack the full coupling of k -dependent density modes, they are known to accurately reproduce many important features of fully microscopic MCT, including the qualitative scaling behavior near the critical point (52, 64). Following the full derivation described in the Supplementary Material, we arrive at the following equation:

$$\dot{\phi}(t) + \Omega^2(T)\phi(t) + \lambda(T) \int_0^t \phi^2(t-s)\dot{\phi}(s)ds = 0. \quad [1]$$

Here, $\phi(t)$ represents the normalized intermediate scattering function $F(k_0, t)/S(k_0)$, the dots denote derivatives with respect to time, and the temperature-dependent functions $\Omega^2(T)$ and $\lambda(T)$ are given by

$$\begin{aligned} \Omega^2(T) &= \frac{k_B T}{m_0} \frac{k_0^2}{S(k_0; T)} \\ &\equiv C_1 \frac{T}{S(k_0; T)} \end{aligned} \quad [2]$$

and

$$\begin{aligned} \lambda(T) &= \frac{\sqrt{3}}{16\pi^2} \frac{k_B T}{\rho m} k_0^3 [S(k_0; T) - 1]^2 \\ &\equiv C_2 T [S(k_0; T) - 1]^2 \end{aligned} \quad [3]$$

where m_0 is the particle mass. Based on the numerical vitrimer simulation data of Fig. 3(c), we consider temperature-dependent growth profiles of $S(k_0)$ of the form

$$S(k_0; T) = 1 + (T^{-1})^{1/\nu}, \quad [4]$$

where the exponent ν can be tuned to represent different growth behaviors upon supercooling. Physically, this exponent thus captures the non-trivial role of the vitrimer bulk density, effectively enabling a tuning from steric-repulsion-dominated to topology-dominated interactions. For simplicity we solve Eqs. 1-3 for $C_1 = C_2 = 1$.

Figure 5 shows the Angell plot of the calculated relaxation times τ_ν [defined via $\phi(\tau_\nu) \equiv e^{-1}$] as a function of inverse temperature. Note that the temperature scale in Fig. 5 is normalized with respect to the corresponding schematic-MCT transition temperatures T_c , i.e. the temperatures at which τ_ν diverges. For comparison, we also plot the predictions of the widely employed F_2 model (52, 64), a simple schematic MCT model which assumes that $\Omega^2 \sim \text{constant}$ and $\lambda(T) \sim T^{-1}$. We use the fastest relaxation time of the F_2 model as our unit of time to enable a fair comparison between the different models.

There are two important conclusions to be drawn from the results in Fig. 5. First, an inflection point appears in $\tau_\nu(T)$ when using our ν -dependent form of the structure-factor peak. That is, there is an initial high-temperature regime in which the relaxation time grows only weakly, but as the temperature further decreases, a power-law divergence emerges sufficiently close to the critical point T_c . Note that such an inflection point is absent in the conventional MCT F_2 model. Although our microscopic MCT calculations for (super)strong vitrimers in Fig. 2(b) do not exhibit any power-law behavior at the temperatures at which we can adequately equilibrate our samples ($T > T_g$), our schematic MCT analysis reveals that an MCT power-law divergence indeed exists, but only at temperatures sufficiently close to the MCT critical point. We therefore unambiguously conclude that, for our vitrimer simulation model, the MCT critical point must lie below the simulated glass transition temperature T_g .

The second main observation is that, by increasing the value of ν —which physically corresponds to a weaker temperature variation of $S(k_0)$ —, the plateau value of τ_ν at the inflection point is tuned to increasingly large values (see inset of Fig. 5). We now recall that the operational glass transition temperature T_g is defined as the temperature at which τ exceeds a certain threshold value (taken as $10^{4.5}\tau_0$ in simulation). The tunability of ν thus provides an effective means to shift the experimental window of observation, i.e. the temperature regime in which the melt can still be equilibrated, such that only the logarithmic-like growth of τ is manifestly visible. In practice, this implies that an arbitrarily slow growth of $S(k_0)$ can result in an arbitrarily large suppression of the cage effect and manifestly low fragility indices m , as indeed we have found in Fig. 2(d). Overall, this analysis confirms that the remarkably broad, density-controlled fragility range of our vitrimer simulation model can be rationalized—within the context of

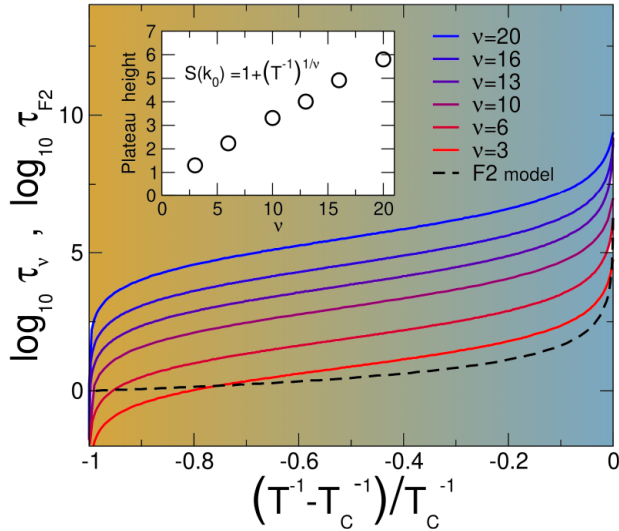


Fig. 5. Angell plots of the relaxation time $\tau_\nu(T)$ as predicted from our schematic MCT model [Eqs. 1–3], assuming a peak growth of the static structure factor $S(k_0)$ as given by Eq. (4) and $C_1 = C_2 = 1$. Different curves correspond to different values of the growth parameter ν . The dashed line indicates the results of the conventional F_2 reference model. The glass transition temperature T_c is defined as the point where the predicted relaxation time strictly diverges. The inset shows the plateau values at the inflection point, i.e. the τ_ν values at the temperature T where the curvature of $\tau_\nu(T)$ changes sign. Note that it grows exponentially with the parameter ν .

first-principles-based MCT—in terms of the broad variation of the growth behavior of $S(k_0)$.

4. Discussion

We have presented a combined numerical and theoretical study of the anomalous fragility of glass-forming vitrimeric networks, a new class of recyclable polymer networks endowed with reversible bond-swap functionality. Our coarse-grained numerical simulation model is composed of star polymers with intrachain attractive harmonic bonds and interchain repulsive interactions; the end segments of the polymer arms are functionalized such that they can undergo reversible bond swaps. Our MD simulations reveal that, by changing the bulk density ρ by a factor of 2–3, the vitrimer fragility at T_g can be tuned from fragile (super-Arrhenius) to strong (Arrhenius) and even superstrong (sub-Arrhenius) behavior. The fragility and corresponding density-dependent tunability are found to be independent of the topology-freezing transition temperature T_v at which all bond-swapping events cease, although the value of T_v does affect the absolute location of the glass-transition line in the (ρ, T) phase diagram.

Surprisingly, we can qualitatively reproduce the entire fragility range using microscopic, fit-parameter-free MCT—a first-principles theory that is conventionally assumed to be only applicable to fragile glass formers. A detailed analysis allows us to trace the microstructural origin of the vitrimer fragility to a single experimental observable: the main peak of the static structure factor. We observe that the strongest vitrimers have the lowest variation of $S(k)$ along the cooling protocol, which is particularly evident for the peak at wavenumber k_0 : the weaker the growth of $S(k_0)$, the stronger the material. We can subsequently rationalize this behavior in terms of a weakening of the cage effect and a change in the vitrimers’ dominant length scale, which switches from

intra- to interchain nearest-neighbor interactions as the density decreases. Finally, based on these microscopic insights, we develop a simplified schematic MCT model that takes into account only the growth behavior of $S(k_0)$. This model not only recovers the qualitative features of our fully microscopic MCT predictions, but it also reveals how our MCT-predicted fragility range can be united with the theory’s well-known fragile power-law divergence near the MCT critical point. The latter lies below the operational glass transition temperature of our simulation model, in the regime where the vitrimer melt has already fallen out of equilibrium. Based on these results, we conclude that MCT is in fact capable of predicting manifestly different fragilities, provided that the MCT critical point lies sufficiently far below the experimental T_g .

Though not remedying the well-documented failures of standard MCT—which ultimately stem from MCT’s mean-field-like approximation for the memory kernel (32, 46, 65)—our work uncovers a hitherto unknown regime in which MCT serves as an accurate first-principles theory of glassy dynamics. This provides a promising basis for further first-principles-based studies of the glass transition, including the development of a Generalized MCT that rigorously goes beyond the mean-field limit (66–69). In future work, it will be interesting to explore how our MCT analysis compares to other non-fragile glass formers such as silica (62, 70–73), and to other glassy materials with two or more competing molecular length scales. Furthermore, the anomalous superstrong fragility may also be rationalized using other theoretical paradigms such as, e.g., the energy landscape (6, 8), which offers an intuitive picture for glassy dynamics in terms of energy-barrier-crossing events. Finally, our findings, in particular the role of the density as a tunable fragility parameter, and the anomalous growth behavior of the main peak of the static structure factor, can be validated in rheological and scattering experiments of vitrimer-like materials. Such a combined theoretical and experimental approach holds exciting potential for the rational structural design of recyclable amorphous plastics with unprecedented dynamical and mechanical performance.

Materials and Methods

Simulation details. Every star polymer is composed of $n = 25$ segments: one central segment and 8 arms of 4 segments each, as depicted in Fig. 1. Nearest-neighbor segments interact through a harmonic potential with equilibrium length equal to the unit of length, and any other segment-segment pair interacts through a repulsive WCA potential with cutoff radius $\sigma = 0.9$. For the end segments of every arm, we further distinguish between two different types, A and B (depicted as red and blue beads in Fig. 1). These segments are capable of forming A-B attractive bonds through a generalized 20-10 Lennard-Jones potential of equilibrium length $2^{1/10}\sigma$ and bond energy ϵ . We study a mixture of $N_1 = 600$ stars with 7 type-A ends and 1 type-B end segment, and $N_2 = 300$ stars of the opposite composition (1 type-A and 7 type-B ends) for a total of $N = 22500$ segments. Since for all temperatures considered the bond energy ϵ is larger than the thermal energy $k_B T$, all simulations result in a fully bonded network of 900 star polymers with 2700 A-B bonds and 1800 unbounded ends of the majority type (A); the latter can act as initiators for the swap reactions. Compared to Ref. (37), the model was optimized in order to avoid its rigidification at the topological transition T_v (3) by changing the mixture ratios to reduce the number of intra-star bonds. In this condition, the mechanism driving the dynamical arrest is the standard glass transition, so that the system can relax and reach equilibrium even below T_v .

Vitrimeric bond-swap functionality is implemented by imposing both a 1-to-1 bond condition and a (A-B-A or B-A-B) swap mechanism through an additional three-body potential $v_{ijk}^{(3)}$ (42):

$$v_{ijk}^{(3)} = \lambda \epsilon v_{ij}^{\text{bond}}(r_{ij}) v_{ik}^{\text{bond}}(r_{ik}), \quad [5]$$

where the indices i, j, k run over all possible A-B-A or B-A-B triplets, and v_{ik}^{bond} represents the A-B (generalized Lennard-Jones) pair potential. The parameters are chosen to set swappable bonds of length $r_{\text{min}} = 2^{1/10} \sigma \approx 0.54$ and energy $\epsilon \gg k_B T$. The three-body parameter λ effectively controls the swap rate through the energy barrier $\Delta E_{\text{swap}} = \epsilon(\lambda - 1)$. Full details for the potentials can be found in (37, 42, 74). In the low-temperature limit, swaps are required to reach true equilibrium configurations (75), hence we keep $\Delta E_{\text{swap}} = 0$ during equilibration. The inclusion of swap events also accelerates the process of initial self-assembly (76).

Our simulations are performed in a cubic box with periodic boundary conditions within the *NVT* ensemble. We start the network assembly and equilibration process at a relatively high temperature, $T = 0.2$, for several values of ρ . The bulk density ρ is controlled by changing the size of the cubic box. Our production runs consist of $n_t = 10^6$ to 10^8 timesteps with a step size of $dt = 10^{-3}$, starting from the equilibrated samples. From the configuration at intermediate density $\rho = 1.5$ and $T = 0.2$ we measure the relaxation time $\tau_0 = 0.06$ that will be used as reference for the dynamics. We then proceed to decrease the temperature T of every sample and repeat the same protocol. To confirm that our calculations are done at equilibrium, we have verified that the temperature T , pressure P , and the structure factor $S(k)$ are constant along the production runs; to exclude any aging effects we have compared the self-intermediate scattering function at the beginning and at the end of each simulation run, as show in Fig. S1. For every state point we have performed 2 to 5 independent runs. All simulations are performed using the HOOMD-blue package (77).

We calculate the self- and collective intermediate scattering functions $F_s(k, t)$ and $F(k, t)$, as well as the static structure factors $S(k)$, from our MD production runs at different ρ and T . Rather than using the full 25×25 partial correlation matrices, we invoke the site-averaged approximation, which effectively replaces specific monomer-monomer correlations with mean-field averaged ones. This choice of approximation is motivated by scattering experiments in which it is not possible to distinguish between the contributions of different monomers. Within the context of MCT, the site-averaged approximation has also been successfully applied to polymers (25, 26, 43–45, 56), leading to a first-principles-based confirmation of the Rouse model (78). Since we are interested only in qualitative results, we set the form factor $w(k)$ (55, 79) to 1, thus ignoring the change in the conformation of our polymers. In Fig. S7 of the Supplementary Material, we test the effect of the form factor by explicitly including it in our microscopic MCT calculations for a superstrong data set. The results confirm that the predicted fragility is unaffected by our site-averaged approximation.

Mode-Coupling Theory. We solve the microscopic MCT equation-of-motion for the self- and collective intermediate scattering functions $F_s(k, t)$ and $F(k, t)$ in the overdamped limit (33, 65). For the collective dynamics the MCT equation reads

$$\dot{F}(k, t) + \Omega^2(k) F(k, t) + \int M(k, t - \tau) \dot{F}(k, \tau) d\tau = 0 \quad [6]$$

where $\Omega^2(k) = k^2 k_B T / [m_0 S(k)]$ is the bare frequency term, T the temperature, and m_0 the particle mass. The memory kernel in Eq. 6 is approximated in the standard MCT formalism as

$$M(k, t) = (k_B T / m_0) \rho / (16\pi^3) \int d\mathbf{q} |V_{\mathbf{k}-\mathbf{q}, \mathbf{q}}|^2 \cdot \left[S(\mathbf{q}) S(|\mathbf{k}-\mathbf{q}|) F(\mathbf{q}, t) F(|\mathbf{k}-\mathbf{q}|, t) \right], \quad [7]$$

where the vertex function $V_{\mathbf{k}-\mathbf{q}, \mathbf{q}} = \hat{\mathbf{k}} \mathbf{q} c(\mathbf{q}) + \hat{\mathbf{k}}(\mathbf{k}-\mathbf{q}) c(|\mathbf{q}-\mathbf{k}|)$, with $\hat{\mathbf{k}} = \mathbf{k}/|\mathbf{k}|$ and $c(\mathbf{q})$ the direct correlation function, is determined by static quantities only. For $F_s(k, t)$ a similar MCT equation applies,

$$\dot{F}_s(k, t) + \Omega_s^2(k) F_s(k, t) + \int M_s(k, t - \tau) \dot{F}_s(k, \tau) d\tau = 0, \quad [8]$$

with $\Omega_s^2(k) = k^2 k_B T / m_0$ and

$$M_s(k, t) = (k_B T / m_0) \rho / (16\pi^3) \int d\mathbf{q} (\hat{\mathbf{k}} \mathbf{q})^2 c(\mathbf{q})^2 F(\mathbf{q}, t) F_s(|\mathbf{k}-\mathbf{q}|, t). \quad [9]$$

The equations are solved under the standard boundary conditions $\dot{F}(k, 0) = 0$, $F(k, 0) = S(k)$, $\dot{F}_s(k, 0) = 0$, and $F_s(k, 0) = 1$. Time propagation is performed using Fuchs' algorithm (80, 81), starting with a step size of $dt = 10^{-6}$ that doubles every 32 steps. The k -dependent integral in the memory kernel is solved by a double Riemann sum on an equidistant grid of 100 wavenumbers, ranging from $k = 0.2$ to $k=40$ (82).

ACKNOWLEDGMENTS. It is a pleasure to thank Francesco Sciortino, Barbara Capone, David Reichman, and Kees Storm for interesting discussions and Stefano Fine for technical support. L.M.C.J. acknowledges the Netherlands Organization for Scientific Research (NWO) for support through a START-UP grant.

- Montarnal D, Capelot M, Tournilhac F, Leibler L (2011). *Science* 334(6058):965–968.
- Capelot M, Montarnal D, Tournilhac FF, Leibler L (2012). *J Am Chem Soc* 134(18):7664–7667.
- Denissen W, Winne JM, Du Prez FE (2016). *Chem. Sci.* 7(1):30–38.
- Angell CA (1995). *Science* 267(5206):1924–1935.
- Mattsson J, et al. (2009). *Nature* 462(7269):83–86.
- Sussman DM, Paoluzzi M, Marchetti MC, Manning ML (2018). *EPL (Europhysics Lett.)* 121(3):36001.
- Dalle-Ferrier C, et al. (2016). *J. Chem. Phys.* 145(15).
- Debenedetti PG, Stillinger FH (2001). *Nature* 410(6825):259.
- Dyre JC (2006). *Rev. Mod. Phys.* 78(3):953–972.
- Cavagna A (2009). *Phys. Rep.* 476(4-6):51–124.
- Tarjus G (2011) in *Dyn. Heterog. Glas. Colloids, Granul. Media*, eds. L. Berthier, G. Biroli, J.-P. Bouchaud, L. Cipelletti, van Saarloos W. (Oxford University Press), pp. 39–67.
- Berthier L, Biroli G (2011). *Rev. Mod. Phys.* 83(2):587–645.
- Binder K, Kob W (2011). (World Scientific).
- Charbonneau P, Kurchan J, Parisi G, Urbani P, Zamponi F (2017). *Annu. Rev. Condens. Matter Phys.* 8(1):265–288.
- Saika-Voivod I, Poole PH, Sciortino F (2001). *Nature* 412(6846):514.
- Sastry S, Debenedetti PG, Stillinger FH (1998). *Nature* 393(554):554–557.
- Krausser J, Samwer KH, Zaccone A (2015). *Proc. Natl. Acad. Sci.* 112(45):13762–13767.
- Ozawa M, Kim K, Miyazaki K (2016). *J. Stat. Mech. Theory Exp.* 2016(7):74002.
- Gnan N, Zaccarelli E (2019). *Nat. Phys.* 15(7):683–688.
- Asai M, Cacciuto A, Kumar SK (2018). *ACS Cent. Sci.* 4(9):1179–1184.
- Yan L, Düring G, Wyart M (2013). *Proc. Natl. Acad. Sci.* 110(16):6307–6312.
- Van Der Scheer P, Van De Laar T, Van Der Gucht J, Viassopoulos D, Sprakel J (2017). *ACS Nano* 11(7):6755–6763.
- Philippe AM, et al. (2018). *Phys. Rev. E* 97(4):1–5.
- Williams I, Oğuz EC, Bartlett P, Löwen H, Patrick Royall C (2015). *J. Chem. Phys.* 142(2):24505.
- Chong SH, Aichele M, Meyer H, Fuchs M, Baschnagel J (2007). *Phys. Rev. E* 76(5):51806.
- Aichele M, Chong SH, Baschnagel J, Fuchs M (2004). *Phys. Rev. E* 69(6):14.
- Scopigno T, Ruocco G, Sette F, Monaco G (2003). *Science* 302(5646):849–852.
- Royall CP, Williams SR (2015). *Phys. Rep.* 560:1–75.
- Xia X, Wolynes PG (2000). *Proc. Natl. Acad. Sci.* 97(7):2990–2994.
- Tarjus G, Kivelson SA, Nussinov Z, Viot P (2005). *J. Phys. Condens. Matter* 17(50):R1143–R1182.
- Sausset F, Tarjus G, Viot P (2008). *Phys. Rev. Lett.* 101(15):155701.
- Götze W (2008). (OUP Oxford) Vol. 143.
- Gotze W, Sjogren L (1992). *Rep Prog Phys* 55(3):241–376.
- Kob W (2002) in *Slow Relaxations nonequilibrium Dyn. Condens. matter. Les Houches-Ecole d'Ete Phys. Theor.*, eds. J. Barrat, M. Feigelman, J. Kurchan, Dalibard J. (Springer Berlin Heidelberg).
- Götze W (1999). *J. Phys. Condens. Matter* 11(10A):A1–A45.
- Mauro NA, Blodgett M, Johnson ML, Vogt AJ, Kelton KF (2014). *Nat. Commun.* 5:1–7.
- Ciarella S, Sciortino F, Ellenbroek WG (2018). *Phys. Rev. Lett.* 121(5):1–11.
- Likos CN (2006). *Soft Matter* 2(6):478–498.
- Watzlawek M, Likos CN, Löwen H (1999). *Phys. Rev. Lett.* 82(26):5289–5292.
- Likos CN, et al. (1998). *Phys. Rev. Lett.* 80(20):4450–4453.
- Gu Y, et al. (2017). *Proc. Natl. Acad. Sci.* 114(19):4875–4880.
- Sciortino F (2017). *Eur. Phys. J. E* 40(1):3.
- Chong SH, Fuchs M (2002). *Phys. Rev. Lett.* 88(18):185702.
- Schweizer KS, Fuchs M, Szamel G, Guenzia M, Tang H (1997). *J. Environ. Monit.* 1(2):23N–25N.
- Schweizer KS, Curro JG (1997). (Advances in Chemical Physics) Vol. 98, pp. 1–142.
- Janssen LMC (2018). *Front. Phys.* 6:97.
- Charbonneau P, Ikeda A, Parisi G, Zamponi F (2011). *Phys. Rev. Lett.* 107(18):1–5.
- Maxwell JC (1864). *London, Edinburgh, Dublin Philos. Mag. J. Sci.* 27(182):294–299.
- Calladine CR (1978). *Int. J. Solids Struct.* 14(2):161–172.
- Phillips JC, Thorpe MF (1985). *Solid State Commun.* 53(8):699–702.
- Rovigatti L, Nava G, Bellini T, Sciortino F (2018). *Macromolecules* 51(3):1232–1241.

52. Leutheusser E (1984). *Phys. Rev. A* 29(5):2765–2773.
53. Landes FP, Biroli G, Dauchot O, Liu AJ, Reichman DR (2019). *arXiv:1906.01103*.
54. Coslovich D (2012). *J. Chem. Phys.* 138(12):1–9.
55. Frey S, et al. (2015). *Eur. Phys. J. E* 38(2):11.
56. Baschnagel J, Varnik F (2005). *J. Phys. Condens. Matter* 17(32):R851—R953.
57. Charbonneau P, Ikeda A, Parisi G, Zamponi F (2012). *Proc. Natl. Acad. Sci.* 109(35):13939–13943.
58. Charbonneau P, Jin Y, Parisi G, Zamponi F (2014). *Proc. Natl. Acad. Sci.* 111(42):15025–15030.
59. Roldán-Vargas S, Rovigatti L, Sciortino F (2017). *Soft Matter* 13(2):514–530.
60. Brambilla G, et al. (2009). *Phys. Rev. Lett.* 102(8):85703.
61. Parisi G, Zamponi F (2010). *Rev. Mod. Phys.* 82(1):789–845.
62. Horbach J, Kob W (2001). *Phys. Rev. E* 64(4):41503.
63. Sciortino F (2008). *Eur. Phys. J. B* 64(3-4):505–509.
64. Bengtzelius U, Gotze W, Sjolander A (1984). *J. Phys. C Solid State Phys.* 17(33):5915–5934.
65. Reichman DR, Charbonneau P (2005). *J. Stat. Mech. Theory Exp.* 2005(2):1–23.
66. Szamel G (2003). *Phys. Rev. Lett.* 90(22):228301.
67. Janssen LMC, Mayer P, Reichman DR (2014). *Phys. Rev. E* 90(5):52306.
68. Janssen LMC, Reichman DR (2015). *Phys. Rev. Lett.* 115(20):1–9.
69. Luo C, Janssen LMC (2019). *arXiv:1909.00428*.
70. Horbach J, Kob W (1999). *Phys. Rev. B* 60(5):3169.
71. Voigtmann T, Horbach J (2008). *J. Phys. Condens. Matter* 20(24):244117.
72. Sciortino F, Kob W, Walter K, Kob W (2001). *Phys. Rev. Lett.* 86(4):648.
73. Berthier L (2007). *Phys. Rev. E* 76(1):11507.
74. Ciarella S, Ellenbroek WG (2019). *Coatings 2019, Vol. 9, Page 114* 9(2):114.
75. Oyarzún B, Mognetti BM (2018). *J. Chem. Phys.* 148(11):114110.
76. Gnan N, Rovigatti L, Bergman M, Zaccarelli E (2017). *Macromolecules* 50(21):8777–8786.
77. Glaser J, et al. (2015). *Comput. Phys. Commun.* 192:97–107.
78. Doi M, Edwards SF (1988). (Oxford University Press).
79. Wittmer JP, et al. (2007). *Europhys. Lett.* 77(5):56003.
80. Fuchs M, Götze W, Hofacker I, Latz A (1991). *J. Phys. Condens. Matter* 3(1991):5047–5071.
81. Flenner E, Szamel G (2005). *Phys. Rev. E* 72(3):1–15.
82. Franosch T, Fuchs M, Götze W, Mayr MR, Singh AP (1997). *Phys. Rev. E* 55(6):7153–7176.

DRAFT